

Determination of Hemoglobin Oxygen Saturation from Turbid Media Using Reflectance Spectroscopy with Small Source-Detector Separations

MAUREEN JOHNS, COLE A. GILLER, and HANLI LIU*

Joint Program of Biomedical Engineering, University of Texas Arlington/Southwestern Medical Center at Dallas, Arlington, Texas 76019 (M.J., H.L.); and Department of Neurological Surgery, University of Texas Southwestern Medical Center at Dallas, Dallas, Texas 75390 (C.A.G.)

In this study, we present an empirically modified diffusion model determining hemoglobin oxygen saturation from turbid media using steady-state, broadband (500–600 nm) reflectance with source-detector separations of a few hundred micrometers. Development of this model was conducted using Monte Carlo simulations, a gold standard modeling technique for predicting the behavior of light propagation through turbid media. Hemoglobin oxygen saturation levels of 0 and 100% at different blood concentrations were studied. Nonlinear curve fitting was used to extract the hemoglobin oxygen saturation values from the reflectance spectra, producing errors of 5% between the simulated curves and the model for both saturation cases. Further validation was performed using liquid-tissue phantoms containing intralipid and blood. Curve fitting between the *in vitro* data and the model produced errors of less than 2%. This validated model was then used to extract saturation values from *in vivo* reflectance spectra of the human index finger and human brain tissues. This empirically modified diffusion model provides the possibility of extracting local hemoglobin oxygen saturation from blood-perfused turbid media using reflectance data measured with a small source-detector separation probe.

Index Headings: Hemoglobin oxygen saturation; Reflectance spectroscopy; Empirically modified diffusion model; Absorption; Monte Carlo simulations.

INTRODUCTION

Optical methods have been used to measure blood flow,¹ tissue oxygenation,^{2,3} hemoglobin concentration,⁴ and hemoglobin oxygen saturation.^{5,6} Optical probes with small source-detector separations (ρ), also referred to as needle-like probes, have become increasingly popular for use in cancer diagnosis,⁷ tissue distinction⁸ or classification,⁹ and drug delivery monitoring.¹⁰ Quantification of biological tissues using a needle-like probe is highly desirable, and several studies in this direction have been reported.^{10–12} Furthermore, such types of probes can be useful during minimally invasive procedures and surgeries. It is important to develop quantitative methods that can be employed to obtain physiological parameters from optical measurements with a needle-like probe.

The diffusion approximation has been largely used in recent years for understanding near-infrared (NIR) light (650–900 nm) propagation through turbid media, including biological tissues, and for quantifying optical properties of tissues.^{13,14} The solutions of the diffusion equation^{15–17} have been well validated by experimental measurements or Monte Carlo simulations under the follow-

ing conditions: (1) ρ is much larger than transport mean free paths (mfp's, also referred to as z_0 in this paper); and (2) the absorption coefficient (μ_a) of the measured tissue is much smaller than its reduced scattering coefficient (μ_s'), i.e., $\mu_a \ll \mu_s'$. The reduced scattering coefficient (or the absorption coefficient) is a measure of the mean distance traveled by light prior to being scattered (or absorbed). These diffusion approaches do not work for needle-like probes because ρ of the probes is on the same order as the mfp's, and they do not work in the visible range because the magnitudes of μ_a and μ_s' of tissue in the visible range are on the same order.

In this paper, we will demonstrate that the conventional diffusion model for optical reflectance, R , can be empirically modified and simplified to an analytical expression for the reflectance with a very small ρ as a function of wavelength, λ , i.e., $R = R(\lambda)$ in the visible range. We will further validate the model by using Monte Carlo simulations and *in vitro* measurements. Specifically, we will review the conventional diffusion approximation in the following section and briefly describe the Monte Carlo simulations and corresponding results thereafter, showing the inconsistencies between the conventional diffusion theory and simulations when $\rho = 0.125$ mm. We then show how to modify and simplify the conventional model to accommodate small source-detector separations. To validate the theoretical results, we conducted *in vitro* measurements. We will describe the *in vitro* and *in vivo* experimental procedures used for the theoretical validation and for showing practical examples, respectively. Finally, we present the theoretical and experimental (both *in vitro* and *in vivo*) results, followed by a discussion and conclusion.

TISSUE OPTICAL PROPERTIES AND CONVENTIONAL DIFFUSION THEORY

Major chromophores that absorb light in living tissues are oxygenated and deoxygenated hemoglobin molecules (HbO_2 and Hb , respectively) with distinct optical-absorption spectra in the visible and NIR range. Myoglobin and cytochromes are additional absorbing molecules found in tissues within these wavelength ranges. Although the absorption spectrum of myoglobin is similar to that of hemoglobin, myoglobin is found only within skeletal and cardiac muscle cells; therefore, it can be excluded from our studies since our primary application is for the brain tissues. Cytochrome absorption is pronounced within the visible wavelength range; however, the tissue concentra-

tion is several orders of magnitude less than hemoglobin concentrations.^{18,19} Thus, hemoglobin absorption remains greater within the visible and NIR range²⁰ by a factor of 8; therefore, absorption due to cytochromes was omitted from the algorithm described here. This omission may contribute to a 5% error associated with the Monte Carlo simulation results.

When ρ is on the order of a few hundred micrometers, sufficient photons can be transmitted or backscattered through blood-perfused turbid media and can be detected in both the visible and the NIR ranges. The detected signal depends strongly on concentrations of HbO_2 and Hb and shows more prominent features in the visible range than in the NIR range. This is because within the visible range, the values of μ_a and μ_s' are on the same order of magnitude, so the backscattered light is characterized equally by both absorption and scattering effects. The spectral dependence of μ_a for blood-perfused tissues can be written as Eq. 1:

$$\mu_a = a \cdot \epsilon_{\text{HbO}_2}(\lambda) + b \cdot \epsilon_{\text{Hb}}(\lambda) \quad (1)$$

where λ is the wavelength in nm; a and b represent concentrations of HbO_2 and Hb , respectively; and $\epsilon_{\text{HbO}_2}(\lambda)$ and $\epsilon_{\text{Hb}}(\lambda)$ are extinction coefficients²⁰ for HbO_2 and Hb at λ , respectively. It is known that the spectral dependence of μ_s' of tissue is weak and can be approximated as Eq. 2:

$$\mu_s' = -c \cdot \lambda + d \quad (2)$$

where c and d are two tissue-dependent parameters.²¹

An approximation to transport theory is diffusion theory, which allows one to determine the optical properties of turbid media, such as *in vivo* tissues, from steady-state diffuse reflectance, R , where R is the diffuse photon flux escaping from the tissue/boundary interface (i.e., at $z = 0$). The reflectance is given as R in Eq. 3:^{16,22}

$$R(\rho, z_0) = \frac{I_0}{4\pi} \left[z_0 \left(\mu_{\text{eff}} + \frac{1}{r_1} \right) \frac{\exp(-\mu_{\text{eff}} r_1)}{r_1^2} + (z_0 + 4AD) \times \left(\mu_{\text{eff}} + \frac{1}{r_2} \right) \frac{\exp(-\mu_{\text{eff}} r_2)}{r_2^2} \right] \quad (3)$$

where $r_1 = \sqrt{(z_0^2 + \rho^2)}$, $r_2 = \sqrt{(z_0 + 4AD)^2 + \rho^2}$, $\mu_{\text{eff}} = \sqrt{\mu_a/D}$, I_0 is an overall amplitude factor, D is the diffusion coefficient and equal to $D = 1/[3 \times (\mu_a + \mu_s')]$, z_0 is the depth of the isotropic point source of a pencil beam and equal to $z_0 = 1/\mu_t = 1/(\mu_a + \mu_s')$, and A is a constant related to the internal reflection. In the diffusion regime, (i.e., when $\mu_a \ll \mu_s'$), Eq. 3 is consistent with spatially resolved Monte Carlo simulations with ρ larger than ~ 1 mm.¹⁶ An improved solution is also available for more accurate characteristics of tissue optical properties for $\rho > 1$ mm.²³ However, our current question is whether these solutions can be empirically modified to model the reflectance with small ρ (0.1–1.0 mm) in the visible light range, where μ_a and μ_s' values of blood-perfused tissues have similar magnitudes. In order to address this question, we employed Monte Carlo simulations to assist with theory modifications.

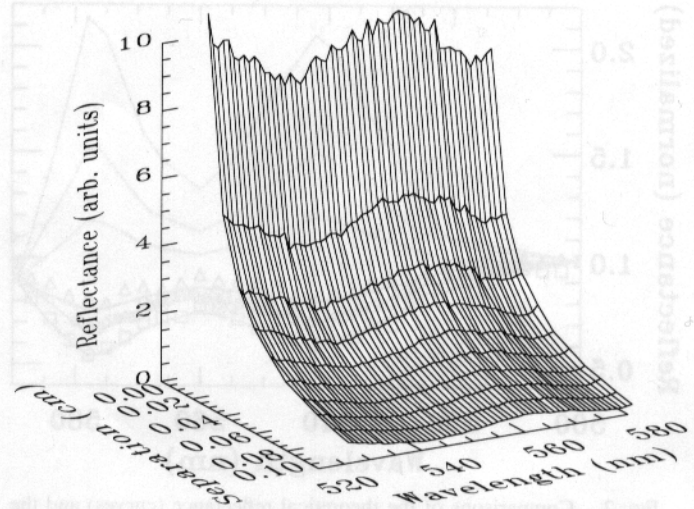


FIG. 1. Monte Carlo simulations for steady-state reflectance from 520 to 580 nm with source-detector separations of 0.0 to 0.1 cm. The values of reflectance are not normalized. The procedures and input parameters are mentioned in the text.

MONTE CARLO SIMULATIONS

During the past decade, Monte Carlo (MC) simulations²⁴ have served as a gold standard method for predicting the behavior of light within turbid media, such as tissues. These simulations have been used to accurately predict and characterize light scattering,^{25–28} absorption,^{29,30} and optical properties^{31,32} from *in vivo* tissues. Furthermore, MC simulations between 500 and 600 nm^{8,12} were used to model optical reflectance spectra from human tissues. Figure 1 is a 3-dimensional plot showing the simulated MC reflectance versus both wavelength (520–580 nm) and source-detector separation (0.0–0.1 cm) for a hemoglobin oxygen saturation value of 100%. This figure demonstrates that optical reflectance within the visible range has strong spatial and spectral dependence. In our approach, we will use the spectral features to modify the diffusion model for tissue properties.

The simulation input parameters^{33,34} were $g = 0.9$ and $n = 1.38$. Two variables, c ($= 0.0065 \text{ cm}^{-1}$) and d ($= 14.5 \text{ cm}^{-1}$), were substituted into Eq. 2 to obtain the reduced scattering coefficients at each wavelength. The effective hemoglobin concentrations in the detected volume were chosen to be 100, 200, and 400 μM for 100% hemoglobin oxygen saturation ($s\text{O}_2$) with $a = 100, 200$, and $400 \mu\text{M}$ and $b = 0 \mu\text{M}$. Those concentration values were selected because 200 μM is an average hemoglobin concentration in tissue vasculature. This average hemoglobin concentration value is calculated in the following manner: the absorption coefficient is defined as $\mu_a = [C] \cdot \epsilon$, where $[C]$ is the concentration of hemoglobin and ϵ is the extinction coefficient. Average values of the absorption coefficient and extinction coefficient in the NIR range for tissues are 0.1 cm^{-1} and $0.46 \text{ mM}^{-1} \cdot \text{cm}^{-1}$, respectively. By substituting these into the given equation, the average hemoglobin concentration in tissues is found to be approximately 200 μM . Furthermore, in simulations for $s\text{O}_2 = 0\%$, we used deoxyhemoglobin values of 100, 200, and 400 μM at $a = 0 \mu\text{M}$ and $b = 100, 200$, and $400 \mu\text{M}$, respectively.

Spectral comparisons were made between the simulat-

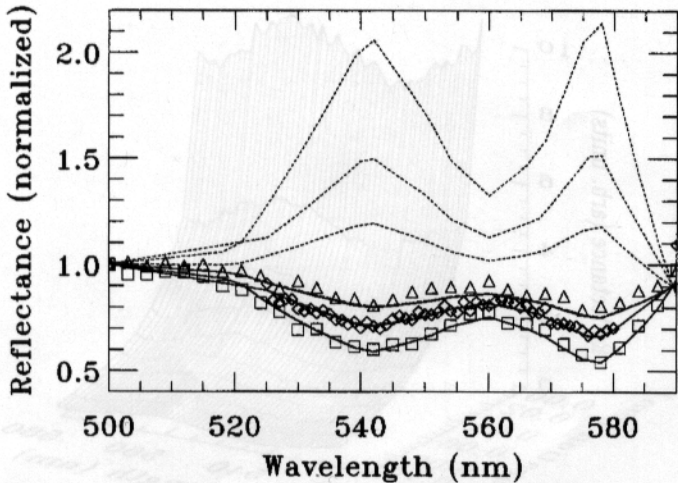


Fig. 2. Comparisons of the theoretical reflectance (curves) and the MC simulations (symbols) with oxyhemoglobin concentration values $a = 100 \mu\text{M}$ (triangles), $200 \mu\text{M}$ (diamonds), and $400 \mu\text{M}$ (squares) and deoxyhemoglobin concentration values $b = 0$ at $\rho = 0.125 \text{ mm}$. The upper dashed curves were calculated using Eq. 3 without modification; the three solid curves were calculated using Eq. 3 with modifications of $D = 1/3\mu_s'$ and $z_0 = 1/\mu_s'$, at corresponding HbO_2 concentrations. The lower dashed curves were calculated using Eq. 5. Curves calculated from Eq. 3, with modifications, and from Eq. 5 are almost too close to be differentiated visually.

ed and theoretical reflectance data using Eq. 3 for $a = 100, 200, \text{ and } 400 \mu\text{M}$ and $b = 0$ (i.e., $\text{sO}_2 = 100\%$) at $\rho = 0.125 \text{ mm}$, as shown in Fig. 2. All data points were normalized at 500 nm . Large inconsistencies between the simulated data (symbols) and theoretical data (upper dashed curves) are observed here. This is what one expects since the diffusion approximation does not hold when μ_a values are large and/or ρ is small. Moreover, simulations with $\text{sO}_2 = 0\%$ at $a = 0 \mu\text{M}$ and $b = 100, 200, \text{ and } 400 \mu\text{M}$ follow the same inconsistencies (data not shown) as those obtained for the oxyhemoglobin case. Therefore, modification of the conventional diffusion equation is needed to accommodate small separations.

MODIFICATIONS AND SIMPLIFICATIONS OF DIFFUSION THEORY

A debate exists regarding which of the following D values is more correct in describing light diffusion in turbid media: $D = 1/(3 \times \mu_s')$ or $D = 1/(3 \times \mu_t') = 1/[3 \times (\mu_a + \mu_s')]$.^{35,36} Hielscher³⁷ demonstrated that when $D = 1/(3 \times \mu_t') = 1/[3 \times (\mu_a + \mu_s')]$, the results depend strongly on the source-detector separation. However, when calculations are performed using $D = 1/(3 \times \mu_s')$, the results are not as strongly dependent on the source-detector separation. Mathematically, when $\mu_a \ll \mu_s'$, the absorption coefficient can be ignored from D , so the above expressions for D are basically identical when using NIR light. However, $D = 1/(3 \times \mu_t') = 1/[3 \times (\mu_a + \mu_s')]$ and $D = 1/(3 \times \mu_s')$ may lead to different results in light reflectance when using visible light, where μ_a and μ_s' are on the same order of magnitude.

Empirically, after we (1) used $D = 1/3\mu_s'$ and (2) modified the depth of the isotropic source from 1 transport mfp, $z_0 = 1/\mu_t'$ to 1 transport scattering mfp, $z_0 = 1/\mu_s'$, Eq. 3 matches the MC data very well when ρ is less than

a few hundred micrometers. The calculated curves using Eq. 3 with $D = 1/3\mu_s'$ and $z_0 = 1/\mu_s'$ are also shown in Fig. 2 (lower solid curves) and exhibit good consistency between the simulated data and the modified model for all respective concentrations.

Furthermore, Eq. 3, with new z_0 and D values, can be simplified for small ρ . Let us take the limit of small ρ and arrive at the following equation:

$$R(z_0) = R(\rho \rightarrow 0, z_0)$$

$$= \frac{I_0 \mu_s'^2}{4\pi} \left\{ (1+k)\exp(-k) + \frac{1}{\left(1 + \frac{4A}{3}\right)^2} \right. \\ \left. \times \left[1 + \left(1 + \frac{4A}{3}\right)k \right] \exp\left[-k\left(1 + \frac{4A}{3}\right)\right] \right\} \quad (4)$$

where $k = z_0 \times \mu_{\text{eff}} = \sqrt{(3 \times \mu_a)/\mu_s'}$ with $z_0 = 1/\mu_s'$ and $\mu_{\text{eff}} = \sqrt{3 \times \mu_a \times \mu_s'}$. Further calculations have proven³⁸ that magnitudes of the first term of Eq. 4 are at least 90% larger than those of the second term when the source-detector separation is less than 0.5 mm (with $\mu_s' < 30 \text{ cm}^{-1}$), and the relative refractive index, n , of the tissue-air interface is equal to or larger than 1.33 in both the visible and the NIR ranges. Thus, the second term of Eq. 4 can be ignored, and a simplified diffusion model for the steady-state broadband reflectance measured with $\rho < 0.5 \text{ mm}$ can be obtained approximately as:

$$R(\mu_a, \mu_s') = \frac{I_0 \mu_s'^2}{4\pi} \left(1 + \sqrt{\frac{3 \times \mu_a}{\mu_s'}} \right) \exp\left(-\sqrt{\frac{3 \times \mu_a}{\mu_s'}}\right) \quad (5)$$

where μ_a and μ_s' values are wavelength dependent and can be expressed as Eqs. 1 and 2, respectively. The calculated curves using Eq. 5 are plotted in Fig. 2 for all three HbO_2 concentrations (lower dashed lines), but they are too close to be differentiated visually from those obtained using the modified Eq. 3.

In order to obtain hemoglobin oxygen saturation values from optical reflectance measurements, the following steps are taken:

- (1) Raw reflectance spectra were measured from *in vitro* or *in vivo* experiments.
- (2) To eliminate spectral effects from the fiber, light source, and instrument response, the measured raw spectra were divided by a calibration curve taken from a standard reference sample. This step gives the R values in Eq. 5.
- (3) The R term in Eq. 5 is then normalized to the first point at $\lambda = 500 \text{ nm}$ (R_0) to eliminate I_0 and to generate Eq. 6:

$$\frac{R}{R_0} = \frac{\mu_s'^2 \times \left(1 + \sqrt{\frac{3 \times \mu_a}{\mu_s'}} \right) \cdot \exp\left(-\sqrt{\frac{3 \times \mu_a}{\mu_s'}}\right)}{\mu_{s_0}'^2 \times \left(1 + \sqrt{\frac{3 \times \mu_{a_0}}{\mu_{s_0}'}} \right) \cdot \exp\left(-\sqrt{\frac{3 \times \mu_{a_0}}{\mu_{s_0}'}}\right)} \quad (6)$$

where μ_{s_0}' and μ_{a_0} are the reduced scattering coeffi-

cient and absorption coefficient of the measured sample, respectively, at 500 nm.

- (4) We substitute Eqs. 1 and 2 into Eq. 6 to generate Eq. 7:

$$\frac{R}{R_0} = \left[(d - c \times \lambda)^2 \right. \\ \times \left(1 + \sqrt{\frac{3 \times [a \times \epsilon_{\text{HbO}_2}(\lambda) + b \times \epsilon_{\text{Hb}}(\lambda)]}{(d - c \times \lambda)}} \right) \\ \times \exp \left(- \sqrt{\frac{3 \times [a \times \epsilon_{\text{HbO}_2}(\lambda) + b \times \epsilon_{\text{Hb}}(\lambda)]}{(d - c \times \lambda)}} \right) \\ \div \left[(d - c \times \lambda_0)^2 \right. \\ \times \left(1 + \sqrt{\frac{3 \times [a \times \epsilon_{\text{HbO}_2}(\lambda_0) + b \times \epsilon_{\text{Hb}}(\lambda_0)]}{(d - c \times \lambda_0)}} \right) \\ \times \exp \left(- \sqrt{\frac{3 \times [a \times \epsilon_{\text{HbO}_2}(\lambda_0) + b \times \epsilon_{\text{Hb}}(\lambda_0)]}{(d - c \times \lambda_0)}} \right) \left. \right] \quad (7)$$

Because the four parameters, a , b , c , and d , in this equation are not totally independent, they cannot be completely and uniquely fitted using this equation.

- (5) Thus, Eq. 7 was modified to Eq. 8, which contains three independent parameters, $X (= a/d)$, $Y (= b/d)$, and $Z (= c/d)$.

$$\frac{R}{R_0} = \left[(1 - Z \times \lambda)^2 \right. \\ \times \left(1 + \sqrt{\frac{3 \times [X + \epsilon_{\text{HbO}_2}(\lambda) + Y \times \epsilon_{\text{Hb}}(\lambda)]}{(1 - Z \times \lambda)}} \right) \\ \times \exp \left(- \sqrt{\frac{3 \times [X + \epsilon_{\text{HbO}_2}(\lambda) + Y \times \epsilon_{\text{Hb}}(\lambda)]}{(1 - Z \times \lambda)}} \right) \\ \div \left[(1 - Z \times \lambda_0)^2 \right. \\ \times \left(1 + \sqrt{\frac{3 \times [X \times \epsilon_{\text{HbO}_2}(\lambda_0) + Y \times \epsilon_{\text{Hb}}(\lambda_0)]}{(1 - Z \times \lambda_0)}} \right) \\ \times \exp \left(- \sqrt{\frac{3 \times [X \times \epsilon_{\text{HbO}_2}(\lambda_0) + Y \times \epsilon_{\text{Hb}}(\lambda_0)]}{(1 - Z \times \lambda_0)}} \right) \left. \right] \quad (8)$$

Now all parameters in Eq. 8 are known except for parameters X , Y , and Z , which can be determined from experimental data by a non-linear curve fitting procedure. The parameters X , Y , and Z are determined for each measurement. Hemoglobin oxygen saturation is then calculated using fitted parameters of X and Y , where $s\text{O}_2 = X/(X + Y) \times 100 (\%)$. The following sections will describe the procedures and equipment used to validate this empirically modified diffusion model.

MATERIALS AND METHODS

Instrumentation. As shown in Fig. 3, the experimental set-up consisted of a light source, fiber optic probe,

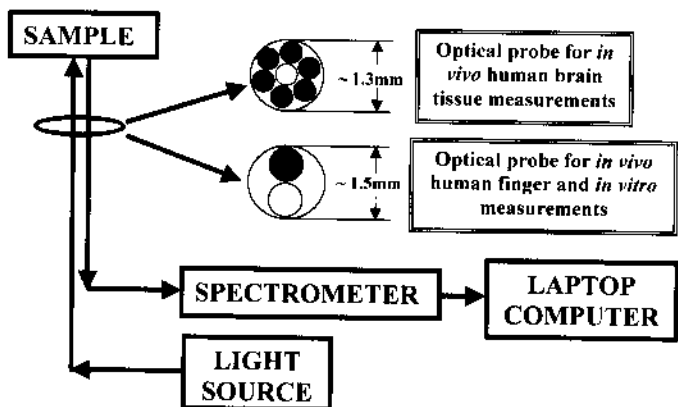
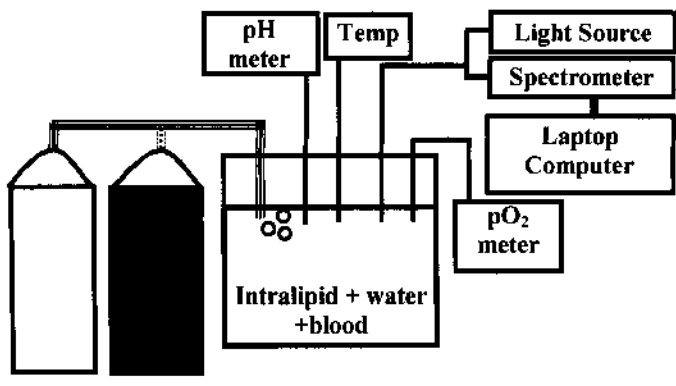


FIG. 3. Instrumentation set-up. The 1.3-mm diameter fiber-optic probe (for *in vivo* human brain tissue measurements) contains one light-delivery fiber (open circle) and six light-collection fibers (solid circles). Each fiber is 100 μm in diameter. The 1.5-mm diameter fiber-optic probe (for *in vivo* human finger and *in vitro* measurements) contains one light-delivery fiber and one light-collection fiber. Each fiber is 400 μm in diameter. The bifurcated probe connects to the light source and spectrometer. The spectrometer connects to a laptop computer via a DAQ card. The reflected signal intensity versus wavelength is displayed on the computer screen.

spectrometer, data acquisition card, and laptop computer. The incident light was generated by a tungsten-halogen light source (LS-1, Ocean Optics, Inc., Dunedin, FL). The spectrometer (SD2000, Ocean Optics, Inc., Dunedin, FL) had a wavelength grating from 350–850 nm and was used to convert the optical signal to an electrical signal. That signal was passed, via the DAQ-700 card, to the laptop computer that displayed the results. LabVIEW programming software (National Instruments, Austin, TX) was used as the software interface between the spectrometer and laptop to display the optical reflectance information in real time. The fiber-optic probe contained two leads, one connected to the light source and the second connected to the spectrometer.

The experimental studies were performed using two distinct bifurcated fiber-optic probes with different internal configurations. For the *in vivo* human brain studies, we used an optical probe containing one 100- μm diameter fiber in the center for light delivery surrounded by six 100- μm diameter fibers for light collection. The source-detector separations were 0.1–0.2 mm. Since this probe was designed specifically for *in vivo* human brain studies and was required to be sterilized and stored in the hospital, it was not available for laboratory use. For the *in vivo* human finger and *in vitro* studies, we used another optical probe containing two separate 0.4-mm diameter fibers for light delivery and light collection, respectively. In this case, the source-detector separation was ~ 0.4 mm. In both cases, other than the regular fiber cladding, no additional cladding or other spacers were added to separate the light collection and light detection fibers. Since each optical reflectance signal is divided by a calibration curve (discussed further in the Data Analysis section), all effects from the fiber, light source, and instrumentation have been removed. Originally, the motivation for using two kinds of fibers was to study any influence of fiber geometry on the measured results. Because of the calibration procedure, using two different



Oxygen Nitrogen

Fig. 4. Experimental set-up for *in vitro* measurements. The same instrumentation detailed in Fig. 3 is shown here. The gas tubing is connected to the oxygen tank to oxygenate the solution and to the nitrogen tank to deoxygenate the solution, respectively. In addition to the optical reflectance, pH, temperature, and pO_2 are also recorded.

fiber optic probe configurations did not alter the experimental results.

In Vitro Measurements Using Liquid-Tissue Phantoms. *In vitro* measurements were performed to validate the modified diffusion model given in Eq. 8. As shown in Fig. 4, the fiber-optic probe, a pH/temperature probe, a nitrogen/oxygen delivery tube, and pO_2 needle and reference electrodes were secured in a parafilm-covered beaker. Each instrument was calibrated prior to use. The pH/temperature probe was calibrated using a pH = 7.0 solution of calibrating buffer. The pO_2 needle electrode and reference electrode were calibrated using 150 ml of 0.9% sodium chloride solution. Air (21% oxygen) and nitrogen (0% oxygen) were used as the two calibrating gases.

Initially, the parafilm-covered beaker contained a 100 mL solution of 1% intralipid. A 1% intralipid solution was chosen because this concentration yields light scattering properties similar to those found in human tissues. Nitrogen was bubbled into the intralipid solution to remove all oxygen. Once the pO_2 meter displayed a consistent reading of 0 mmHg, 1.5 mL of rabbit blood (hemoglobin concentration \approx 90 μ M) was added while the nitrogen continued to bubble slowly. The blood contained heparin in order to prevent clotting. Several spectra of optical reflectance were recorded immediately following the addition of the blood. The pH, temperature, and pO_2 values were also noted.

After the deoxygenated solution was measured, the nitrogen was turned off and air (21% oxygen) was slowly bubbled into the solution. Air was continuously bubbled until a pO_2 value of 100 mmHg was reached. This pO_2 value corresponds to a sO_2 value of 100% based on the hemoglobin oxygen dissociation curve.³⁹ Optical reflectance spectra, pH, temperature, and pO_2 were recorded at this point. Three *in vitro* measurements were conducted and produced a total of 15 files for 0% oxygenation and 22 files for 100% oxygenation. Each measurement produced similar, reproducible results. It is also important to notice that the calculated results are not sensitive to added hemoglobin concentrations within the measurement range.

In Vivo Measurements from Human Index Finger. The optical probe was placed against the surface of the

skin of a human index finger such that the tip of the probe was just touching the skin. Virtually no pressure was applied from the probe to the skin in order to keep local hemoglobin oxygen levels unperturbed. Reflectance measurements were obtained from this regularly oxygenated state. In addition, while keeping the probe in the same location on the finger, pressure was then applied from the probe to the skin causing the local region of tissue to become deoxygenated. Reflectance measurements were also obtained from this deoxygenated state.

In Vivo Measurements from Human Brain Tissues.

All optical reflectance measurements from living, human brain tissues were obtained during regularly scheduled neurosurgeries with prior patient consent. Prior to the neurosurgical procedure, a stereotactic frame was securely fixed to the patient's head. This frame provided accurate placement for both the surgical and optical probes. The optical probe was designed with the same dimensions as the surgical probe to provide compatibility with the available surgical instrumentation.

Numerous optical reflectance measurements have been taken from human brain tissues *in vivo* using the current instrumentation and a thin (1.3-mm o.d.) fiber-optic probe.⁴⁰ During the *in vivo* measurements, the sterile optical probe was inserted through the stereotactic frame and advanced to the surface of the brain. The probe was manually advanced in 1 mm increments from the surface of the brain to a depth of approximately 80 mm. Reflectance spectra were recorded at each 1 mm increment; therefore, spectra could be seen from gray matter, white matter, and cerebrospinal fluid in the ventricle. The track of the fiber optic probe was compared to post-operative MRI and CT scans to precisely identify the anatomical structures of the deep brain and correlate these structures with the optical output.⁴⁰ Two optical spectra were chosen for this study that had been identified as either gray matter (6 mm deep) or white matter (30 mm deep) post-operatively.

Data Analysis, Curve Fitting Procedure and Calibration. Equation 8 was entered into Interactive Data Language (IDL) programming software (Research Systems, Boulder, CO). A non-linear curve fitting algorithm, Levenberg–Marquardt method, was used to perform the fitting procedure.⁴¹ X, Y, and Z were the fitted output parameters after the theory had been fit with the experimental data. This routine was used to calculate oxygen saturation values of blood-perfused tissue from a reflectance spectrum.

First, we used the normalized reflectance spectra from Monte Carlo simulations to validate the empirically modified diffusion model and fitting algorithm. Simulation results from deoxygenated (0%) and oxygenated (100%) blood-perfused tissues were selected, as used in Fig. 2, and entered into the curve-fitting routine. The values of X, Y, and Z were determined when small fitting errors and a close match between the fitted curves and simulation results occurred. Second, further confirmation was obtained by using *in vitro* normalized spectra that produced sO_2 values of approximately 0% and 100%, as indicated by the pO_2 measurement. (An oxygen dissociation curve was used to convert the pO_2 values to sO_2 .) The output sO_2 values from the curve fitting routine were compared to the expected values to substantiate the per-

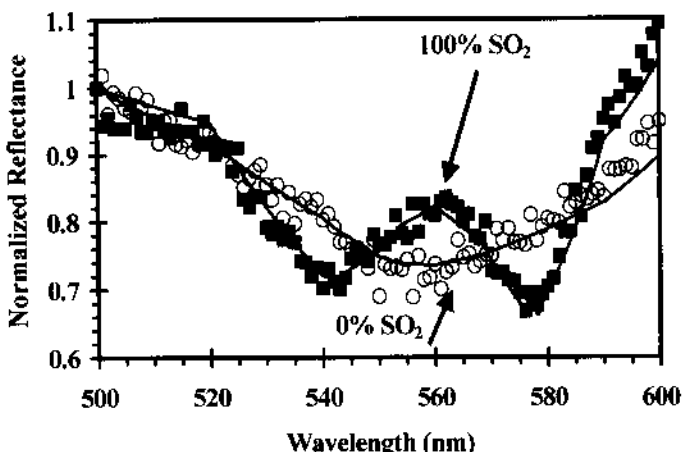


FIG. 5. Monte Carlo data for 100% SO_2 (filled squares) and 0% SO_2 (open circles) solutions and fitted theoretical curves from Eq. 8 (solid lines) with $p = 125 \mu\text{m}$. For both cases, total hemoglobin concentrations were $200 \mu\text{M}$.

formance of the model and the fitting algorithm. After validation, *in vivo* spectra from both the human index finger and the human brain tissues were selected to calculate oxygen saturation values of the finger and the gray and white matter of the brain. The results obtained from all curve-fitting procedures are presented in the following section.

All data that were entered into IDL were calibrated. In order to calibrate the data, a calibration curve was obtained from a white reference sample (WS-1, Diffuse Reflectance Sample, Ocean Optics, Dunedin, FL) following data collection during each experiment. The white reference sample has a thermoplastic surface that is >99% reflective between 200–1100 nm. The calibration curve, also known as the reference curve, includes all spectral effects of the light source, fiber optics, and any other instrument responses excluded from the tissue studied. The measured reflectance data were then calibrated (i.e., the reflectance spectrum divided by the calibration sample spectrum) and entered into the curve-fitting routine to obtain the sO_2 values.

RESULTS

Monte Carlo Simulations. In general, Monte Carlo simulation results have been used as a gold standard when predicting optical reflectance based on scattering and absorption properties of a turbid medium. In our case, Monte Carlo simulations were performed at each 1 nm increment from 500 to 600 nm for both 0% and 100% oxygenated blood-perfused tissues. These spectral curves were used as input data for IDL. Ideally, the fitting routine should produce saturation values close to 0% and 100% for the respective cases. The curve fitting results, as shown in Fig. 5, produced sO_2 values of 5% and 95% for 0% and 100% hemoglobin oxygen saturation, respectively. Therefore, the modified diffusion model for small source-detector separations with the curve-fitting routine produced a 5% error. Furthermore, simulations for $\text{sO}_2 = 0\%$ with values of $a = 0 \mu\text{M}$ and $b = 100$ and $400 \mu\text{M}$ (data not shown) followed the same consistency as that obtained for the $\text{sO}_2 = 100\%$ case.

In Vitro Experimental Data. *In vitro* data used to val-

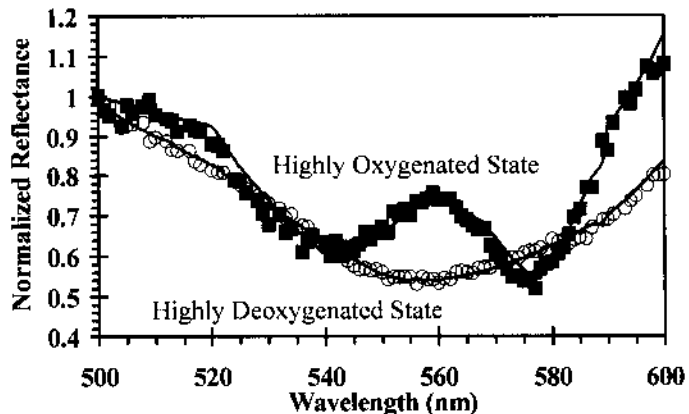


FIG. 6. *In vitro* data (symbols) and curve-fitting results (solid lines). Open circles were obtained from the data at 0 mmHg (deoxygenated), and filled squares were obtained from the data at 90 mmHg (oxygenated). The fitted sO_2 values are 1.4% and 95%, respectively.

idate the model were obtained through laboratory measurements, as detailed in the last section. An oxygen dissociation curve was used to convert the measured pO_2 values (mmHg) to sO_2 values (%). Ideally, the sO_2 (%) values obtained from the dissociation curve using the measured pO_2 values should be equal to those obtained from the optical reflectance measurement.

Figure 6 shows the data obtained from a 100% hemoglobin oxygen saturation solution. The *in vitro* data were selected at $\text{pO}_2 = 90 \text{ mmHg}$, which corresponds to a highly oxygenated hemoglobin solution. According to the dissociation curve, a pO_2 value of 90 mmHg at pH equal to 7.3 corresponds to an oxygen saturation of 95%. The *in vitro* data match closely with the fitted theoretical curve. The curve-fitting results produced a saturation value of 95%. Figure 6 also shows the data obtained from an *in vitro* spectral curve selected at $\text{pO}_2 = 0 \text{ mmHg}$, which corresponds to a highly deoxygenated hemoglobin solution. The curve-fitting results yielded a saturation value of 1.4% with an error of 1.4%.

In Vivo Human Index Finger Data. Once the model and the curve-fitting routine were validated, they were used to determine the oxygen saturation values from various *in vivo* tissue spectra. The instrumentation shown in Fig. 3 and the two-fiber *in vitro* optical probe were used to obtain optical reflectance measurements from the index finger of two volunteers. The oxygen saturation values were then calculated from the reflectance spectra.

Figure 7 shows the measured and fitted data for both the oxygenated and the deoxygenated states of the finger. The normally oxygenated curve shown produced a saturation value of 78%, while the oxygen saturation value for the deoxygenated state was 41%. These values seem reasonable based on the expected values of oxygenated and deoxygenated blood-perfused tissues. After multiple repeatable measurements ($n = 7$), we obtained $\text{sO}_2\%$ values of $77\% \pm 4\%$ and $42\% \pm 5\%$ (mean value \pm standard deviation) for the normally oxygenated state and the deoxygenated state of the finger, respectively. The latter values were dependent on the amount of pressure applied to the probe. It is expected that the pressure applied locally on a tissue occluded blood supply and thus decreased the local amount of oxyhemoglobin concentra-

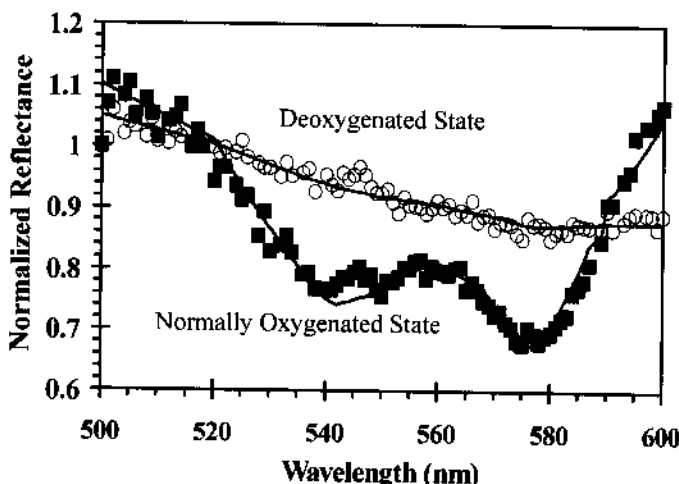


FIG. 7. Optical reflectance data measured from normally oxygenated (filled squares) and deoxygenated (open circles) states of a human index finger. Solid lines represent fitted curves. The fitted sO_2 values are 78% and 41% for regularly oxygenated and deoxygenated states, respectively.

tion, resulting in the presence of deoxyhemoglobin. Thus, ischemia may occur locally with sufficient pressure, but further studies will be needed to know if this process occurs before all of the blood is expressed from the tissue.

The data obtained for local hemoglobin oxygenation levels in a human finger can contain a certain degree of uncertainty as compared to the *in vitro* measurements. Deviations can result from variance in the pressure exerted by the probe on the finger, variance in local oxygenation levels of the finger itself, and variance from person to person depending on such factors as the skin color and room temperature. Kakihana et al.⁴² presented hemoglobin oxygen saturation data obtained from human fingers in various temperature conditions. Their results from human fingers showed a heterogeneous mixture of regions of low oxygenation ($43.9\% \pm 7.8\%$) and high oxygenation ($63.0\% \pm 7.1\%$) at room temperature. Our results presented in this section are in good agreement with those given by Kakihana et al.

In Vivo Human Brain Tissue Data. Spectra from human brain tissues were taken from more than fifty patients who signed consent forms. The measurements were taken from the surface of the brain to a depth of approximately 7 cm. In principle, gray matter has an increased blood volume and contains a higher concentration of oxyhemoglobin; therefore, the model can be valid in obtaining hemoglobin oxygen saturation of gray matter. Conversely, white matter has more myelin fiber tracts, a decreased blood volume, and a lower concentration of oxygenated hemoglobin; thus, the modified diffusion model might not work well for white matter. Figure 8 shows an *in vivo* optical reflectance spectrum from gray matter at a depth of 6 mm within a human brain. After fitting the model with the spectrum from gray matter, we obtained an oxygen saturation value of 53%, in this case. After similar calculations from five other gray matter spectra, we obtained $sO_2\%$ values of $35\% \pm 16\%$ for gray matter, including both from the surface and from certain depths of the human brain. Detailed information is given in Table I. As a comparison, the oxygen saturation for the 30-

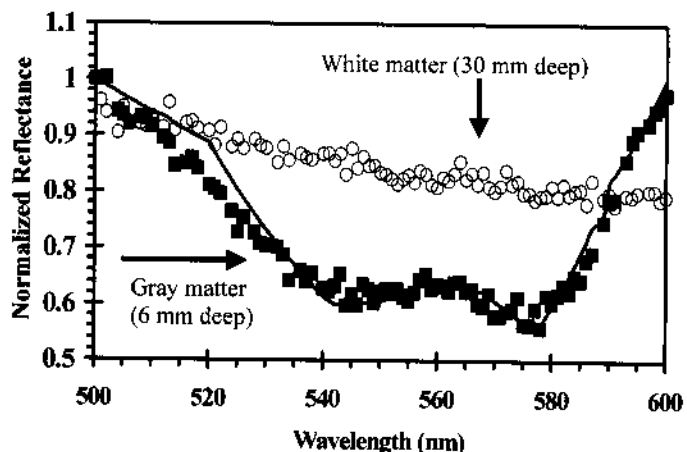


FIG. 8. Optical reflectance data from living, human brain tissues. Filled squares represent gray matter data at 6 mm depth, and open circles represent white matter data at 30 mm depth. The solid curve represents the fitted result with a sO_2 value of 53% for gray matter.

mm-deep white matter curve was calculated to be 28%; however, this value is considered unreliable due to the limited hemoglobin concentration in white matter.

DISCUSSION AND CONCLUSIONS

By modifying D and z_0 in the conventional diffusion model and comparing it to the MC simulations in the wavelength range of 500–600 nm, we demonstrated throughout this paper that the empirically modified diffusion solution can be used to: (1) model steady-state broadband reflectance obtained with a small source-detector separation, and (2) quantify sO_2 values of blood-perfused turbid media, such as tissues. We need to point out that this methodology requires the calibrated spectrum to be normalized at a particular wavelength. In addition, we have noted in our studies that the empirically modified Eq. 3 is not valid as a model for spatially resolved reflectance with multiple ρ 's of 0.1–1.0 mm. In other words, the modified diffusion model cannot match well with the reflectance measured with ρ 's from 0.1 mm to 1.0 mm at a fixed wavelength. This suggests that the empirically modified diffusion model can work well only at a fixed small ρ (< a few hundred micrometers) for the broadband reflectance from 500 nm to 600 nm and normalized at a certain wavelength (e.g., at 500 nm in our case).

The modified calculations presented in this paper have used $D = 1/(3 \times \mu_s')$ and $z_0 = 1/\mu_s'$. These two equations

TABLE I. Hemoglobin oxygen saturation (sO_2) of gray matter from *in vivo* human brain tissues.

Subject number	Position (below the surface of the brain)	sO_2 (%)
1	0 mm	26
1	1 mm	24
1	2 mm	14
2	6 mm	53 (Fig. 8)
3	0 mm	36
4	12 mm	54
Mean (n = 6)		35
Standard Deviation		16

can easily be obtained from the conventional diffusion approximation when using the NIR light (700–900 nm), where μ_a is much less than μ_s' , and thus μ_a can be eliminated from the D and z_0 expressions. When using the visible light, however, there are no mathematical or physical reasons to ignore μ_a since μ_a and μ_s' in this wavelength range are on the same order of magnitude. So far, it is unclear to us why elimination of μ_a in D and z_0 can produce good consistency between the empirically modified diffusion model and the Monte Carlo simulations as well as the *in vitro* experimental results. Further theoretical studies are desirable to provide useful and solid support for our empirically modified diffusion model.

Verification of the modified diffusion model was performed by validating Eq. 8, which contains relative oxygenated and deoxygenated hemoglobin concentrations (i.e., $X = a/d$, $Y = b/d$). Thus, if Eq. 8 is used for sO_2 calculations, the measured medium should be a blood-perfused sample in order to assure the accuracy of the method and the fitting algorithm. It has been observed in our studies that the deviation between the MC data and Eq. 8 increases as the hemoglobin concentration decreases. We have noticed that as hemoglobin concentrations increase, not only do the relative errors between the simulations and Eq. 8 decrease, but also the maximum source-detector separation, ρ , that is valid for the empirically modified model increases. It is expected that Eq. 8 will perform better for well blood-perfused tissues but will encounter certain errors when hemoglobin concentrations are lower than $\sim 100 \mu\text{M}$.

As shown earlier, the curve fitting algorithm involves three output parameters of X , Y , and Z . These parameters contain relative concentrations (a/d , b/d , and c/d), rather than absolute concentrations, (a , b , c , and d) of oxygenated and deoxygenated hemoglobin. The absolute concentration values can be obtained provided the absorption and scattering coefficients at a given point (i.e., specific wavelength) are known for a measured sample. Our next step in this research project includes determining the true concentration values of oxygenated and deoxygenated hemoglobin by taking an accurate calibration measurement from a reference sample with known μ_a and μ_s' values.

Few studies have been reported on oxygen saturation values from living, deep human brain tissues. From the *in vivo* brain tissue measurements, as presented, we observed that the reflectance spectrum from gray matter contained a double-dip spectral feature due to the presence of oxyhemoglobin, while the spectrum from white matter displayed less obvious spectral features. This double-dip feature has occasionally been observed in reflectance spectra from white matter, and, conversely, the double-dip feature has been absent in reflectance spectra from gray matter. It is possible that the spectral differences observed between gray and white matter result from the differences in blood volume between the two tissues and/or in oxygen saturation levels. The analysis for *in vivo* human brain oxygenation results presented here is preliminary and requires further study to examine whether or not both blood volume and oxygen saturation levels can be used as physiological markers for identifying neurological structures in living, deep brain tissues *in vivo*.

Doppenberg et al.⁴³ reported human cortex (gray matter) hemoglobin oxygen saturation values as $77\% \pm 18\%$ (59–95%). The mean sO_2 value for gray matter in our study ($35\% \pm 16\%$) is lower than that given by Doppenberg et al. In their case, the sensor was specifically placed close to an artery, which explains the higher average value of 77%. When the artery was occluded, the sO_2 values changed to $33\% \pm 21\%$ (12–54%). In our case, two sO_2 values of 54% and 53% are in good agreement with those provided by Doppenberg et al., suggesting that our probe may have been close to an artery. The other values (26, 24, 14, and 36%) from our measurement yield $26\% \pm 8\%$ (18–34%). Since these values seem to be a little too low for regular cortex tissues, it is expected that the probe was not next to a blood vessel, but rather in less blood-perfused tissues. Further confirmation for this expectation is underway using animal models.

In conclusion, Monte Carlo simulations and *in vitro* experimental data have been used to support the theoretical model, demonstrating that an empirically modified diffusion model can be used to extract hemoglobin oxygenation levels from reflectance measurements of a blood-perfused turbid medium with small source-detector separations. Following appropriate validation, the model was used to extract blood oxygenation from *in vivo* tissues. The modified diffusion model allows one to extract important physiological information from a single optical reflectance spectrum. The entire methodology can be programmed for a real-time display and incorporated into the operating room during surgeries or biopsies to determine oxygen levels within blood-perfused tissues as well as regions of deoxygenation, such as those found within tumors.

ACKNOWLEDGMENTS

The authors acknowledge support from the Whitaker Foundation Research Grant RG-97-0083 and from the National Institutes of Health Grant R01-NS40874-01. The authors thank Dr. Ralph Mason for use of his laboratory and equipment to conduct the *in vitro* experiments.

1. A. D. Edwards, C. Richardson, P. van der Zee, C. Elwell, J. S. Wyatt, M. Cope, D. T. Delpy, and E. O. R. Reynolds, *J. Appl. Physiol.* **75**, 1884 (1993).
2. D. E. Taylor and S. G. Simonson, *New Horiz.* **4**, 420 (1996).
3. V. Pollard, D. S. Prough, A. E. DeMelo, D. J. Deyo, T. Uchida, and H. F. Stoddart, *Anesth. Analg.* **82**, 269 (1996).
4. K. Isobe, T. Kusaka, Y. Fujikawa, M. Kondo, K. Kawada, S. Yasuda, S. Itoh, K. Hirao, and S. Onishi, *J. Biomed. Opt.* **5**, 283 (2000).
5. G. J. Beilman, K. E. Groehler, V. Lazaron, and J. P. Ortner, *Shock* **12**, 196 (1999).
6. A. T. Minassian, N. Poirier, M. Pierrot, P. Menei, J. C. Granry, M. Ursino, and L. Beydon, *Anesthes.* **91**, 985 (1999).
7. J. R. Mourant, I. J. Bigio, J. Boyer, R. L. Conn, T. Johnson, and T. Shimada, *Lasers Surg. Med.* **17**, 350 (1995).
8. M. Johns, C. A. Giller, and H. Liu, *J. Biomed. Opt.* **3**, 437 (1998).
9. D. A. Benaron, W. Cheong, J. L. Duckworth, K. Noles, C. Nezhad, D. Seidman, S. R. Hintz, C. J. Levinson, A. L. Murphy, J. W. Price, F. W. H. Liu, D. K. Stevenson, and E. L. Kermit, *OSA TOPS* **22**, 30 (1998).
10. J. R. Mourant, T. Johnson, G. Los, and I. J. Bigio, *Phys. Med. Biol.* **44**, 1397 (1999).
11. F. Bevilacqua, D. Piguet, P. Marquet, J. D. Gross, D. Jakubowski, V. Venugopalan, B. Tromberg, and C. Depeursinge, *Proc. SPIE-Int. Soc. Opt. Eng.* **3597**, 540 (1999).
12. M. Johns, C. A. Giller, and H. Liu, *Proc. SPIE-Int. Soc. Opt. Eng.* **3595**, 70 (1999).

13. D. Contini, F. Martelli, and G. Zaccanti, *Appl. Opt.* **36**, 4587 (1997).
14. J. L. Karagiannes, Z. Zhang, B. Grossweiner, and L. I. Grossweiner, *Appl. Opt.* **28**, 2311 (1989).
15. M. S. Patterson, B. Chance, and B. C. Wilson, *Appl. Opt.* **28**, 2331 (1989).
16. T. J. Farrell and M. S. Patterson, *Med. Phys.* **19**, 879 (1992).
17. J. B. Fishkin and E. Gratton, *J. Opt. Soc. Am. A* **10**, 127 (1993).
18. F. G. Hempel, F. F. Jobsis, J. L. LaManna, M. R. Rosenthal, and H. A. Saltzman, *J. Appl. Physiol.* **43**, 873 (1977).
19. F. F. Jobsis, J. H. Keizer, J. C. LaManna, and M. Rosenthal, *J. Appl. Physiol.* **43**, 858 (1977).
20. W. G. Zijlstra, A. Buursma, and W. P. Meeuwesen Van Der Roest, *Clin. Chem.* **37**, 1633 (1991).
21. S. J. Matcher, M. Cope, and D. T. Delpy, *Appl. Opt.* **36**, 386 (1997).
22. J. R. Mourant, T. Fuselier, J. Boyer, T. M. Johnson, and I. J. Bigio, *Appl. Opt.* **36**, 949 (1997).
23. A. Kienle and M. S. Patterson, *J. Opt. Soc. Am. A* **14**, 246 (1997).
24. L.-H. Wang, S. L. Jacques, and L.-Q. Zheng, *Comp. Meth. Prog. Biomed.* **54**, 141 (1997).
25. S. T. Flock, M. S. Patterson, B. C. Wilson, and D. R. Wyman, *IEEE Trans. Biomed. Eng.* **36**, 1162 (1989).
26. S. T. Flock, B. C. Wilson, and M. S. Patterson, *IEEE Trans. Biomed. Eng.* **36**, 1169 (1989).
27. C. M. Gardner, S. L. Jacques, and A. J. Welch, *Lasers Surg. Med.* **18**, 129 (1996).
28. L. Bergougnoux, J. Misguich-Ripault, J.-L. Firpo, and J. Andre, *Appl. Opt.* **35**, 1735 (1996).
29. J. R. Mourant, T. Fuselier, J. Boyer, T. M. Johnson, and I. J. Bigio, *Appl. Opt.* **36**, 949 (1997).
30. B. C. Wilson and G. Adam, *Med. Phys.* **10**, 824 (1983).
31. A. Kienle and M. S. Patterson, *Phys. Med. Biol.* **41**, 2221 (1996).
32. F. Bevilacqua, D. Piguet, P. Marquet, J. D. Gross, B. J. Tromberg, and C. Depeursinge, *Appl. Opt.* **38**, 4939 (1999).
33. A. Kienle, L. Lilge, M. S. Patterson, R. Hibst, R. Steiner, and B. C. Wilson, *Appl. Opt.* **35**, 2304 (1996).
34. F. A. Duck, *Physical Properties of Tissue: A Comprehensive Reference Book* (Academic Press, San Diego, 1990), p. 62.
35. K. Furutsu and Y. Yamada, *Phys. Rev. E: Stat. Phys., Plasmas, Fluids, Relat. Interdiscip. Top.* **50**, 3634 (1994).
36. M. Bassani, F. Martelli, G. Zaccanti, and D. Contini, *Opt. Lett.* **22**, 853 (1997).
37. A. H. Heilscher, R. E. Alcouffe, and R. L. Barbour, *Phys. Med. Biol.* **43**, 1285 (1998).
38. H. Liu, *Appl. Opt.* **40**, 1742 (2001).
39. R. H. Garrett and C. M. Grisham, *Biochemistry* (Harcourt Brace College Publishers, Orlando, 1999), 2nd ed., p. 488.
40. C. Giller, M. Johns, and H. Liu, *J. Neurosurg.* **93**, 498 (2000).
41. W. H. Press, B. P. Flannery, S. A. Teukolsky, and W. T. Vetterling, *Numerical Recipes* (Cambridge University Press, New York, 1986), pp. 521–528.
42. Y. Kakihana, M. Kessler, A. Krug, H. Yamada, T. Oda, and N. Yoshimura, *Microvasc. Res.* **56**, 104 (1998).
43. E. M. R. Doppenberg, J. C. Watson, W. C. Broaddus, K. L. Holloway, H. F. Young, and R. Bullock, *J. Neurosurg.* **87**, 809 (1997).